LETTER

Combined theoretical analysis for plasmon-induced transparency in integrated graphene waveguides with direct and indirect couplings

To cite this article: Qi Lin *et al* 2015 *EPL* **111** 34004

A Letters Journal Exploring the Frontiers of Physics

August 2015

EPL, **111** (2015) 34004
doi: 10.1209/0295-5075/111/34004

www.epljournal.org

Combined theoretical analysis for plasmon-induced transparency in integrated graphene waveguides with direct and indirect couplings

Qi Lin[1], Xiang Zhai[1], Lingling Wang[1(a)], Benxin Wang[2], Guidong Liu[1] and Shengxuan Xia[1]

[1] *School of Physics and Electronics Science, Hunan University - Changsha 410082, China*
[2] *School of Science, Jiangnan University - Wuxi 214122, China*

received 18 May 2015; accepted in final form 29 July 2015
published online 28 August 2015

PACS 42.82.Et – Waveguides, couplers, and arrays
PACS 73.20.Mf – Collective excitations (including excitons, polarons, plasmons and other charge-density excitations)
PACS 78.67.Wj – Optical properties of graphene

Abstract – By taking a graphene nanoribbon as a resonator, we have numerically and analytically investigated the spectral characteristics of plasmon-induced transparency in integrated graphene waveguides. For the indirect coupling, the formation and evolution of the transparency window are determined by the excitation of the super resonances, as well as by the destructive interference and the coupling strength between the two resonators, respectively, while for the indirect coupling, the peak transmission and corresponding quality factor can be dynamically tuned by adjusting the Fermi energy of graphene nanoribbons and the transparency peak shifts periodicity with the round-trip phase accumulated in the graphene waveguide region. Analytical results based on temporal coupled mode theory (CMT) show good consistence with the numerical calculations. Our findings may support the design of ultra-compact plasmonic devices for optical modulating.

Introduction. – Electromagnetically induced transparency (EIT) effect observed in atomic media is the result of a quantum destructive interference between coherent optical transitions [1]. The EIT system promises potential applications in slow light, optical storage and other nonlinear optical processes for its high-Q resonances and drastic normal dispersion [2]. However, its application in practice is greatly hindered by the demanding condition that is required to preserve quantum state coherence. Fortunately, an analogical interference phenomenon of wave functions can occur in classical oscillators systems, and EIT-like behavior can be achieved by designing coherent excitation pathways, including coupled microresonators [3], metamaterials [4], photonic crystal cavities [5] and all-dielectric metasurfaces [6]. Surface plasmon polaritons (SPPs), the collective excitations confined in metal-dielectric interface, have been widely studied in past decades, because they can overcome the traditional diffraction limit and manipulate light in deep-subwavelength domain [7]. The most promising candidate among plasmonic devices for plasmon-induced transparency (PIT) is the metal-insulator-metal (MIM) waveguide, which has been theoretically introduced and experimentally demonstrated in recent studies [8–15]. PIT can be realized in MIM waveguide systems via destructive interference between radiative and dark plasmonic modes [9–12] or near-field coupling between two detuned resonators [13–15]. However, the tuning of plasmon resonance is difficult except for carefully re-optimizing the geometric parameters of the metallic nanostructure, which restrict its further development in integrated optics. Recently, graphene plasmonics [16], with a great diversity of electrical and optical properties such as extreme confinement, active tunability, and low loss, have been introduced to the design of PIT devices [17–20]. For example, graphene-based dolmen structures have been investigated comprehensively, suggesting non-radiative loss reduction [17], substantial slow-light effect [18] and dynamic tuning of transparency window via external fields [17–20]. On the other hand, PIT-like transmission can be achieved in graphene integrated Fabry-Perot (FP) microcavity [21], exhibiting high contrast electro-optic modulations. Furthermore, the destructive interference between radiative and dark plasmonic modes supported by a graphene-based dolmen structure

(a) E-mail: llwang@hnu.edu.cn

can be analytically described by the coupled Lorentz oscillator model [17], and the dynamics of PIT-like modulation in graphene integrated FP microcavity can be accurately evaluated by employing the transfer matrix method [21]. However, very few numerical investigations with uniform analytical description have been performed systematically on the PIT effect in integrated graphene waveguide, although this is very essential for the manipulation of propagating SPPs in deep-subwavelength domain.

In this letter, we numerically and theoretically investigate the EIT-like spectral responses in integrated graphene waveguide. There are two typical physical pictures: direct coupling model consisting of a radiative resonator (directly coupled to the waveguide) and a dark resonator (indirectly coupled to the waveguide through the radiative resonator) [22]; indirect coupling model consisting of two detuned resonators, which is essential for the observation of EIT-like and slow-light effect [23]. By taking a graphene nanoribbon as a resonator first, we introduce direct coupling and indirect coupling PIT schemes consisting of two vertically coupled GNRs with lateral displacement s and multi-GNRs coupled to the side of the graphene sheet waveguide, respectively. It is found that plasmonic resonances and spectral characteristics possess strong dependence on the coupling strength in the direct coupling scenario. For the indirect coupling scenario, it is shown that the peak transmission and corresponding quality factor can be dynamically tuned by adjusting the Fermi energy of graphene nanoribbons and the transparency peak can be modulated periodically by the inter-space between the two resonators. In addition, the multi-peak EIT-like line is also investigated. Analytical results based on temporal coupled mode theory (CMT) show good consistence with the numerical calculations. Our findings may provide guidelines for designing ultra-compact PIT devices.

Theory and simulations. – To start with, the plasmonic resonance characteristics in a graphene nanoribbon resonator (GNR)-coupled waveguide are investigated numerically by using the finite-difference time-domain method (FDTD). As shown in figs. 1(a), (b), a monolayer graphene sheet and graphene nanoribbon with width w_i are separately embedded in the dielectric layer with relative permitivity ε_r [24–26]. When light is impinged from the left port, the highly confined SPPs will be supported and propagate in the graphene sheet which acts as a planar waveguide. The graphene nanoribbon can be treated as a novel resonator, where the plasmonic resonant mode can be excited by means of strong optical coupling to the waveguide and dynamically controlled by gate voltage V_g as shown in fig. 1(a) [16,24,26]. In the mid-infrared region, intraband scattering dominates in highly doped graphene, and its conductivity takes on a Drude-like form $\sigma = je^2E_F/[\pi\hbar^2(\omega + j\tau^{-1})]$, $j = (-1)^{1/2}$. The electron relaxation time is expressed as $\tau = \mu E_F/ev_F^2$, where $v_F = c/300$ is the Fermi velocity and $\mu = 10\,\mathrm{m^2/Vs}$ is the

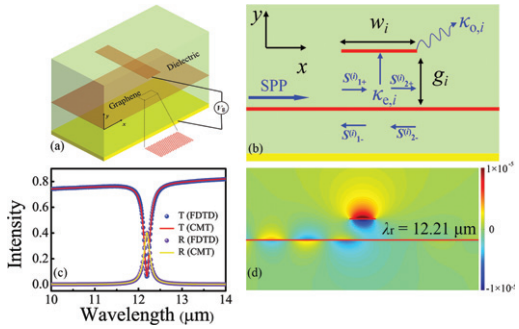

Fig. 1: (Color online) (a) Schematic of the single-GNR–coupled waveguide. The Fermi energy in the graphene nanoribbon can be tuned by external gate voltage V_g. (b) Cross-section diagram of the graphene structure. (c) Numerical calculation (blue balls) and analytical fitting (solid red curves) of the transmission and reflection spectra with width w_i = 100 nm. (d) Field distributions H_z at the resonant wavelength of 12.21 μm (m = 1). The Fermi energy of the graphene sheet and graphene nanoribbon are set as $E_{F0} = 0.17\,\mathrm{eV}$ and $E_{Fi} = 0.16\,\mathrm{eV}$, respectively. The height of the GNR is set as g_i = 100 nm. For the sake of simplicity, the surrounding environment of graphene is assumed to be air $\varepsilon_r = 1$.

DC mobility [24]. The two-dimensional FDTD simulations with a perfectly matched layer (PML) boundary condition are performed, and the graphene layers are modeled as an ultra-thin film with a thickness of 1 nm. The mesh sizes of graphene in the x and y directions are chosen to be 2 nm × 0.1 nm for good convergence of the numerical calculations. The transmission and reflection spectra of the system is presented in fig. 1(c). The first-order resonant mode corresponding to the transmission dip at 12.21 μm is plotted in fig. 1(d). Using the CMT, the energy amplitude a_i for the GNR with resonance frequency ω_i can be expressed as [23]

$$\frac{\mathrm{d}a_i}{\mathrm{d}t} = \left(-j\omega_i - \frac{\omega_i}{2Q_{oi}} - \frac{\omega_i}{2Q_{ei}}\right)a_i + j\sqrt{\frac{\omega_i}{2Q_{ei}}}\left(S_{1+}^{(i)} + S_{2-}^{(i)}\right), \tag{1}$$

where κ_{oi} represents the decay rate of the field due to the internal loss in the GNR, and κ_{ei} is the decay rate due to the energy escape into the waveguide. The decay rates satisfy the relationships $\kappa_{oi} = \omega_i/(2Q_{oi})$, $\kappa_{ei} = \omega_i/(2Q_{ei})$. Here Q_{oi} and Q_{ei} are quality factors related to the internal loss and waveguide coupling strength, $S_{p+}^{(i)}$ and $S_{p-}^{(i)}$ ($p = 1,\ 2$) are the incoming and outgoing SPPs. With energy conservation and time reversal symmetry, the relationships between the amplitudes of the incoming and outgoing SPPs in the waveguide can be described as $S_{2+}^{(i)} = S_{1+}^{(i)} - j(\omega_i/2Q_{ei})^{1/2}a_i$, $S_{1-}^{(i)} = S_{2-}^{(i)} - j(\omega_i/2Q_{ei})^{1/2}a_i$. Combining with boundary conditions $S_{2-}^{(i)} = 0$ and eq. (1), we can obtain analytical expressions for the complex transmission and reflection coefficients of the system,

$$t_i = \alpha\frac{S_{2+}^{(i)}}{S_{1+}^{(i)}} = \alpha\frac{j(\omega_i - \omega) + \omega_i/2Q_{oi}}{j(\omega_i - \omega) + \omega_i/2Q_{oi} + \omega_0/2Q_{ei}}, \tag{2}$$

$$r_i = \alpha \frac{S_{1-}^{(i)}}{S_{1+}^{(i)}} = \alpha \frac{-\omega_i/2Q_{ei}}{j(\omega_i - \omega) + \omega_i/2Q_{oi} + \omega_i/2Q_{ei}}. \quad (3)$$

It should be noted that only the internal loss and waveguide coupling loss of GNR can be considered in CMT. In fact, the dispersion and loss in graphene waveguide give rise to the asymmetric profile and the transmission peak less than unity [25]. Here α is the complex transmission coefficient of the graphene sheet waveguide without GNR, which is introduced to normalize the transmission and reflection efficiency of the single-GNR–coupled waveguide. Similar procedures have been performed in ref. [27]. In addition, it is worth noting that the total loss of the coupled GNRs includes intrinsic loss and waveguide coupling loss. For the electron the relaxation time τ is big enough, according to the dispersion relation of the graphene $k_{spp} = k_0[2\pi\hbar^2\varepsilon_r(\omega + i\tau^{-1})]/(\eta_0 e^2 E_F)$, where $\eta_0 = 377\,\Omega$ is the intrinsic impedance of air. The intrinsic quality factor of the GNR can be estimated from $Q_{oi} = -\mathrm{Re}(k_{spp})/(2\mathrm{Im}(k_{spp}))$. The total quality factor can be estimated from $Q_{ti} = \lambda_{ri}/\delta\lambda$, where $\delta\lambda$ is the FWHM of the reflection spectrum. One can obtain the waveguide coupling loss by subtracting the intrinsic loss from the total loss, namely, $Q_{ei} = Q_{oi}Q_{ti}/(Q_{oi} - Q_{ti})$ [23,25].

We introduce direct coupling and indirect coupling PIT schemes consisting of two vertically coupled GNRs with lateral displacement s and multi-GNRs to the side of the graphene sheet waveguide, respectively, as depicted in figs. 2(a), (b). For the direct coupling scenario, as shown in fig. 2(a), the energy amplitude $a_{1,2}$ can be expressed as [12,22]

$$\frac{\mathrm{d}a_1}{\mathrm{d}t} = \left(-j\omega_1 - \frac{\omega_1}{2Q_{o1}} - \frac{\omega_1}{2Q_e}\right) a_1 + j\sqrt{\frac{\omega_1}{2Q_e}}\,(S_{1+} + S_{2-}) + j\frac{\omega_2}{2Q_c}a_2, \quad (4)$$

$$\frac{\mathrm{d}a_2}{\mathrm{d}t} = \left(-j\omega_2 - \frac{\omega_2}{2Q_{o2}}\right) a_2 + j\frac{\omega_1}{2Q_c}a_1, \quad (5)$$

where $\omega_{1,2}$ is the inherent resonant frequencies of the corresponding GNRs, $\omega_1/(2Q_c) = \kappa_{21}$ and $\omega_2/(2Q_c) = \kappa_{12}$ are the coupling coefficients between the two GNRs. $Q_{o1,2}$, Q_e and Q_c are quality factors related to intrinsic loss, waveguide coupling loss and coupling strength between the two GNRs, respectively. When a time dependence of the form $\exp(j\omega t)$ is assumed and the characteristic equations (4), (5) are solved, the resonance frequency splitting of the coupled system can be deduced as

$$\omega_{r1,2} = \left(\frac{\omega_1 + \omega_2}{2}\right) \pm \mathrm{Re}\,(\Omega_0)\,, \quad (6)$$

where

$$\Omega_0^2 = \frac{\omega_1\omega_2}{(2Q_c)^2} + \left(j\omega_1 - \frac{\omega_1}{2Q_{o1}} - \frac{\omega_1}{2Q_e}\right)\left(j\omega_2 - \frac{\omega_2}{2Q_{o2}}\right) - \left(j\frac{\omega_1 + \omega_2}{2} - \frac{\omega_1}{4Q_{o1}} - \frac{\omega_1}{4Q_e} - \frac{\omega_2}{4Q_{o2}}\right)^2.$$

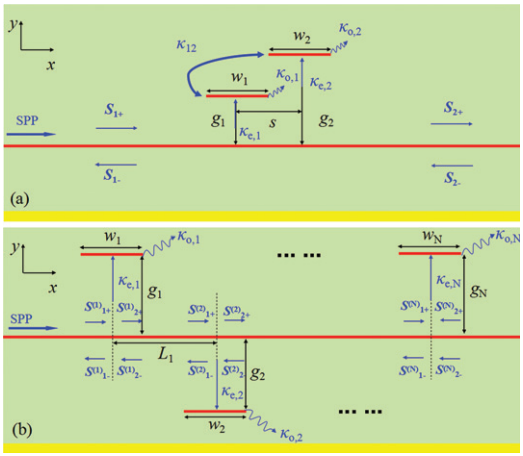

Fig. 2: (Color online) (a) Direct coupling scheme of the graphene sheet waveguide with two GNRs: w_i is the width of the GNR, g_i the height of the GNR, s the lateral displacement between the two GNRs. (b) Indirect coupling scheme of the graphene sheet waveguide with two GNRs: L_i is the interspace between the i-th and $(i+1)$-th $(i = 1, 2, \ldots, N)$ GNRs. The dashed lines indicate the reference planes in the middle of the GNRs. The Fermi energy of GNRs are set as E_{Fi}.

With boundary conditions $S_{2-} = 0$ and $S_{2+} = S_{1+} - j(\omega_i/2Q_{ei})^{1/2}a_i$, $S_{1-} = S_{2-} - j(\omega_i/2Q_{ei})^{1/2}a_i$, we finally arrive at the spectral transmission of the coupled system,

$$T = \left|\alpha\frac{S_{2-}}{S_{1+}}\right|^2 = \left|\alpha\left(1 - \frac{1}{Q_e}\frac{j2\delta_2 + \frac{1}{Q_{o2}}}{\left(j2\delta_1 + \frac{1}{Q_{o1}} + \frac{1}{Q_e}\right)\left(j2\delta_2 + \frac{1}{Q_{o2}}\right) + \left(\frac{1}{Q_c}\right)^2}\right)\right|^2, \quad (7)$$

where $\delta_{1,2} = (\omega - \omega_{1,2})/\omega_{1,2}$ is introduced to normalize the incident frequency ω.

To verify the validity of the analytical model, we numerically calculated the transmission spectra of the direct coupling scenario with different lateral displacement s. As shown in figs. 3(a)–(d), it is found that an obvious transparency window at 12.21 μm emerges and grows in intensity at the original forbidden band when s reaches special values. While for $s = 200$ nm, the strong resonance indicates the efficient excitation of surface plasmons in the first GNR, while the second does not contribute as the GNRs in the two layers are not coupled to each other effectively. To explore physics behind this, we calculated the field distributions H_z at 12.21 μm. It can be seen that a first-order resonance mode is supported in the infinitely long graphene nanoribbon due to the strong coupling to SPPs in the graphene sheet waveguide for $s = 200$ nm. Moreover, most of the energy fails to pass through the waveguide, as plotted in fig. 3(h). As the s is gradually decreased, the resonance mode supported by the first graphene nanoribbon is diminished due to destructive interference and then turns to be excited in the second one,

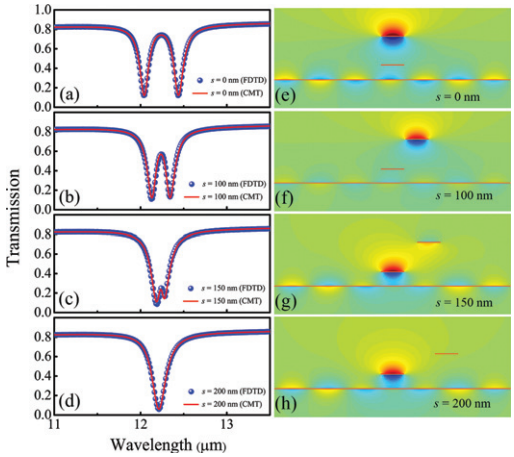

Fig. 3: (Color online) (a)–(d) Transmission spectra calculated by the FDTD method (blue balls) and analytical fittings (solid red curves) by the CMT for different s in the direct coupling scenario. (e)–(h) Field distributions H_z at the transparency wavelength of 12.21 μm. The heights of the two GNRs are set as $g_1 = 100$ nm and $g_2 = 300$ nm. The widths of the two GNRs are fixed to be 100 nm. The Fermi energies in graphene are set to be $E_{F0} = 0.17$ eV, $E_{F1} = E_{F2} = 0.16$ eV.

which could result in an increasing amount of SPPs passing through the waveguide, as plotted in figs. 3(e)–(h). The analytical fitting of eq. (7) to the transmission spectra for different s is presented in figs. 3(a)–(d), exhibiting very good agreement with the numerical calculations. This is the control of the EIT-like transmission spectra, which is different from the method indicated in ref. [24], where the modulation of the transparency window is achieved by changing the vertical distance between the two GNRs, while the different heights g_i of the GNR may slightly affect its resonance frequency [24], which leads to a frequency mismatch between the two GNRs, resulting in the broken symmetry of the EIT-like lines.

From eq. (7), the quality factor $Q_c(\kappa_{21})$ controlled by s between the two GNRs affects the transmission properties of the graphene waveguide, which is similar to the PIT effect in MIM waveguide [22]. With the increase of s from 0 to 200 nm, the coupling coefficient κ_{21} obtained from the analytical fitting is successively deduced from 2.5×10^{12} to 0.48×10^{12} rad/s. As expected, the resonance mode supported by the first GNR is split into two super resonance modes corresponding to the transmission dips at λ_{r1} and λ_{r2}. With the decrease of the coupling strength, λ_{r1} is red-shifted while λ_{r2} is blue-shifted. Each of these numerical results is consistent with the analytical model based on eq. (6). The field distributions E_x are plotted in figs. 4(b), (c) at $\lambda_{r1} = 12.04\,\mu$m, $\lambda_{r2} = 12.44\,\mu$m for $s = 0$ nm. At these wavelengths, the two GNRs are both strongly excited. The near fields in the two GNRs are in phase at 12.44 μm while they are out of phase at 12.04 μm, corresponding to the two super resonances [10]. Actually, both the super resonances are excited at the transparency peak wavelength simultaneously so that the near field is

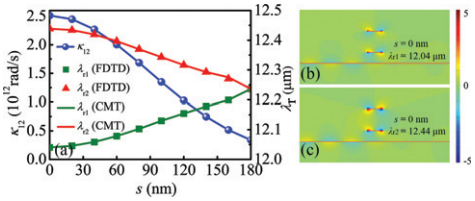

Fig. 4: (Color online) (a) Coupling coefficient κ_{21} (blue balls) as a function of s; resonance wavelength of transmission dips calculated using the CMT (solid curves) and FDTD method (triangles and squares). (b) Field distributions E_x at the transmission dip wavelengths of 12.04, 12.44 μm for $s = 0$ nm.

enhanced in one GNR while prohibited in the other, as shown in fig. 3(e). Hence the formation and evolution of the transparency window are determined by the excitation of the super resonances, as well as by the destructive interference and the coupling strength in the direct coupling scenario, respectively.

For comparison, the indirect coupling scenario shown in fig. 2(b) is also investigated, which is structurally similar to the direct coupling but imply a significantly different physical picture. Combining with eqs. (1)–(3) and $S_{2+}^{(i)} = S_{1+}^{(i)} - j(\omega_i/2Q_{ei})^{1/2}a_i$, $S_{1-}^{(i)} = S_{2-}^{(i)} - j(\omega_i/2Q_{ei})^{1/2}a_i$, the relationship between incoming and outgoing SPP waves of the i-th GNR can be expressed as [23]

$$\begin{bmatrix} S_{1-}^{(i)} \\ S_{2+}^{(i)} \end{bmatrix} = V_i \begin{bmatrix} S_{1+}^{(i)} \\ S_{2-}^{(i)} \end{bmatrix}, \tag{8}$$

where

$$V_i = \begin{pmatrix} -r_i/t_i & \alpha/t_i \\ 1 + r_i/t_i & r_i/t_i \end{pmatrix}.$$

For the indirect coupling configuration, the side-coupled GNRs can be treated as frequency-dependent lossy mirrors, *i.e.* the waveguide regions between the GNRs can be regarded as Fabry-Perot (FP) cavities, and the SPP waves in the graphene waveguide should satisfy the steady-state condition [21,23]

$$\begin{bmatrix} S_{1+}^{(i+1)} \\ S_{2-}^{(i+1)} \end{bmatrix} = M_i \begin{bmatrix} S_{1-}^{(i)} \\ S_{2+}^{(i)} \end{bmatrix}, \tag{9}$$

where

$$M_i = \begin{pmatrix} 0 & e^{j\theta_i} \\ e^{-j\theta_i} & 0 \end{pmatrix}.$$

Here θ_i $(i = 1, 2, \ldots, N-1)$ is the phase difference between the i-th and $(i+1)$-th GNRs, which can be expressed as $\theta_i = \mathrm{Re}(n_{eff})L_i/c$, where $n_{eff} = \pi\varepsilon_0\hbar^2(\omega + j\tau^{-1})/(k_0e^2E_F)$ is the effective index of the graphene waveguide [25]. Thus, the transfer equation of the indirect coupling configuration can be expressed as

$$\begin{bmatrix} S_{1+}^{(i+1)} \\ S_{2-}^{(i+1)} \end{bmatrix} = H \begin{bmatrix} S_{1-}^{(i)} \\ S_{2+}^{(i)} \end{bmatrix}, \tag{10}$$

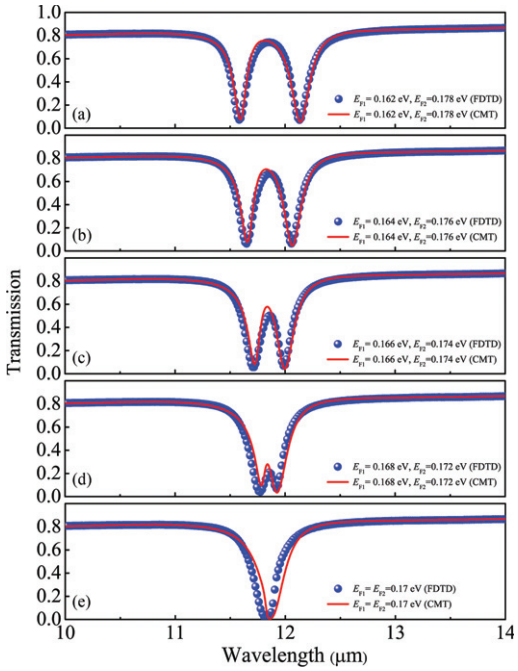

Fig. 5: (Color online) Transmission spectra for the two indirectly coupled GNRs with different frequency detuning corresponding to different Fermi energy E_{Fi} in GNRs. (a) 0.162 and 0.178 eV, (b) 0.164 and 0.176 eV, (c) 0.166 and 0.174 eV, (d) 0.168 and 0.172 eV and (e) 0.170 eV. The widths of GNRs are set as $w_i = 100$ nm and the heights are fixed to be $g_i = 100$ nm. The inter-space is set to be $L_1 = 400$ nm. Numerical and theoretical results are labeled by blue balls and solid red curves, respectively.

where $H = V_N M_{N-1} V_{N-1} M_{N-2}, \ldots, V_2 M_1 V_1$, and the transmittance can be derived as

$$T = \left| \alpha \frac{S_{2+}^{(N)}}{S_{1+}^{(1)}} \right|^2 = \left| \frac{H_{21}H_{12} - H_{22}H_{11}}{H_{12}} \right|^2. \qquad (11)$$

Figure 5 shows the transmission spectra of the dual-GNR–coupled waveguide, suggesting typical EIT-like lineshapes, *i.e.*, a narrow transparency window within the original forbidden band. The resonant wavelength of the two GNRs can be dynamically tuned by adjusting the Fermi energy according to the expression of $\omega_i \propto e\hbar^{-1}(2E_{Fi}(\varepsilon_0 w)^{-1})^{1/2}$ [25]. Based on eq. (11), the transmission efficiency of the dual-GNR–coupled waveguide ($N = 2$) can be deduced to be

$$T_{dual} = \left| \alpha \frac{S_{2+}^{(2)}}{S_{1+}^{(1)}} \right|^2 = \left| \frac{\alpha e^{j2\theta_1} t_1 t_2}{|\alpha|^2 - r_1 r_2 e^{j2\theta_1}} \right|^2, \qquad (12)$$

where $t_{1,2}$ and $r_{1,2}$ based on eqs. (2), (3) are the complex transmission and reflection coefficients of the single-GNR–coupled waveguides with different Fermi energies $E_{F1,2}$. As shown in fig. 5, a transparency window with frequency detuning $|\omega_1 - \omega_2|$ appears at the frequency of $(\omega_1 + \omega_2)/2$. It can be seen that a smaller frequency detuning induces a narrower spectral bandwidth but a reducing peak transmission, indicating a tradeoff between the quality factor and the peak transmission, which is similar to the phase-coupled PIT in a detuned cavity-coupled MIM waveguide [23,27]. Interestingly, the frequency detuning can be dynamically controlled by external gate voltages, which provides a convenient scheme to adjust the quality factor of the transparency window without changing the structural parameters. The theoretical results obtained by eq. (12) are in good agreement with numerical simulations.

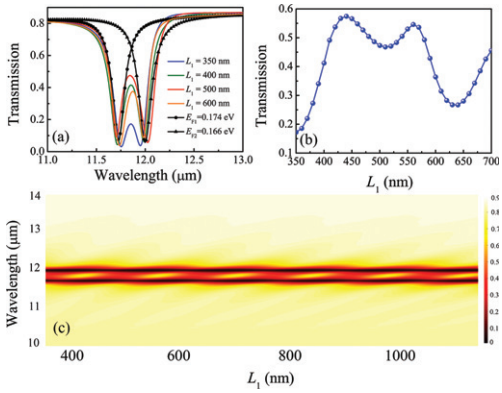

Fig. 6: (Color online) (a) Transmission spectra of the indirect coupling scenario for inter-space $L_1 = 350$, 400, 500 and 600 nm, with $w_1 = w_2 = 100$ nm and $E_{F1} = 0.166$ eV, $E_{F2} = 0.174$ eV. The black solid curves with triangles and circles are the transmission spectra of the single-GNR–coupled waveguide with $E_{F1} = 0.166$ eV and $E_{F2} = 0.174$ eV, respectively. (b) Transmission for different inter-space L_1 at the transparency wavelength of 11.85 μm. (c) Evolution of transmission spectra *vs.* incident wavelength and L_1 obtained by eq. (12).

On the other hand, when light is impinged from the left port, the first-order resonant modes in the two GNRs can be excited simultaneously and the L_1-dependent transparency peak between the separate resonances exhibits a shift in transmission intensity for a fixed frequency detuning, as shown in fig. 6(a), suggesting the coherent and resonant interaction between the two GNRs. According to eq. (12), the transmission efficiency can be further derived as

$$T_{dual} = \left(\frac{|t_1 t_2|}{|\alpha|^2 - |r_1 r_2|} \right)^2 \left(|\alpha|^2 + 4 \left(\frac{\sqrt{r_1 r_2}}{|\alpha|^2 - |r_1 r_2|} \right)^2 \sin^2 \varphi_1 \right)^{-1}, \qquad (13)$$

where φ_1 is one-half of the round-trip phase accumulated in the FP cavity: $\varphi_1 = \mathrm{Arg}[r_1 r_2 \exp(-2j\beta L_1)]/2$. To test this prediction, we numerically calculated the transmission spectrum for different inter-space L_1 at the transparency peak wavelength of 11.85 μm, as shown in fig. 6(b). It can be seen that the transmittance shifts periodicity with the inter-space L_1 (the periodicity is about 150 nm) and the peak values of the transmission spectrum gradually get smaller due to the increase of the intrinsic loss in the waveguide region between the two GNRs.

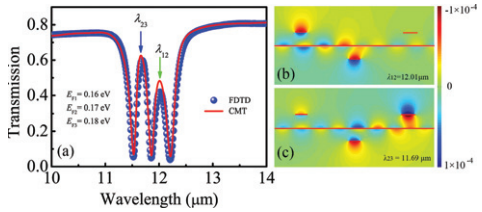

Fig. 7: (Color online) (a) Simulation (blue balls) and theoretical (solid red curve) transmission spectrum of the triple-GNR–coupled waveguide with $w_i = 100\,\text{nm}$, $g_i = 100\,\text{nm}$, $L_1 = L_2 = 100\,\text{nm}$, and $E_{F1} = 0.16\,\text{eV}$, $E_{F2} = 0.17\,\text{eV}$, $E_{F3} = 0.18\,\text{eV}$. Field distributions H_z at the two transparency wavelengths: (b) $\lambda_{12} = 12.01\,\mu\text{m}$ and (c) $\lambda_{23} = 11.69\,\mu\text{m}$.

According to eq. (13), the transmittance gets maximized when one-half of the round-trip phase φ_1 is a multiple of π, *i.e.*, $\sin^2\varphi_1 = 0$. For instance, the real part of the effective refractive index equals 43.07 at $11.85\,\mu\text{m}$, and $\sin^2\varphi_1 = 0.0011$ (0.9967) for $L = 440$ (510) nm corresponds to the maximum (minimum) transmittance of 0.57 (0.46). Figure 6(c) shows the evolution of transmission spectra *vs.* wavelength and L_1 obtained by eq. (12). It is shown that the transmission dips corresponding to the separate resonances remain unchanged, while the transparency peak undergoes periodical modulation, exhibiting good agreement with the numerical simulations.

Finally, a triple-GNR–coupled waveguide is investigated to validate the effectiveness of the theoretical model in multi-GNR–coupled waveguide. When $N = 3$, the transmission efficiency can be obtained as

$$T_{triple} = \left|\alpha\frac{S_{2+}^{(3)}}{S_{1+}^{(1)}}\right|^2 = \left|\frac{\alpha e^{j2(\theta_1+\theta_2)}t_1t_2t_3}{|\alpha|^3-\alpha r_1r_2e^{j2\theta_1}-\alpha r_2r_3e^{j2\theta_2}-\alpha r_1r_3(r_2+t_2)e^{j2(\theta_1+\theta_1)}}\right|^2. \tag{14}$$

As shown in fig. 7(a), the theoretical calculation based on eq. (14) shows good agreement with the numerical simulation. There are two transmission peaks at the wavelengths $\lambda_{12} = 12.01\,\mu\text{m}$ and $\lambda_{23} = 11.69\,\mu\text{m}$ in the transmission spectrum, forming the dual-band EIT-like line. To illustrate the physics behind this, we plotted the field distributions of the transparency wavelengths. An obvious FP resonance is achieved in the waveguide region between the first and second (second and third) GNRs at the wavelength $\lambda_{12} = 12.01\,\mu\text{m}$ ($\lambda_{23} = 11.69\,\mu\text{m}$), as depicted in figs. 7(b), (c), which is consistent with the aforementioned discussion about the dual-GNR–coupled waveguide. It is truly indicated that the indirect coupled model can be further extended to the multi-GNR–coupled situations.

Conclusions. – In conclusion, we have theoretically investigated PIT characteristics using CMT in integrated graphene waveguides with direct and indirect couplings. Numerical simulations verify the theoretical predication and demonstrate that the formation and evolution of the transparency window are attributed to the excitation of the super resonances, as well as to the destructive interference and the coupling strength in the direct coupling scenario, respectively. For the case of indirect coupling, the peak transmission and corresponding quality factor can be dynamically tuned by adjusting the Fermi energy of GNRs. Moreover, the transparency peak shifts periodicity with the round-trip phase accumulated in the waveguide region, which can be quantitatively testified by CMT and FP model. In addition, the indirect coupled model can be further extended to the multi-GNR–coupled situations. Our works may have potential application in the design of ultra-compact plasmonic devices for optical modulating.

* * *

This work was supported by the National Natural Science Foundation of China (Grant Nos. 11074069, 61176116), and the Specialized Research Fund for the Doctoral Program of Higher Education of China (Grant No. 20120161130003).

REFERENCES

[1] Boller K. J. *et al.*, *Phys. Rev. Lett.*, **66** (1991) 2593.
[2] Fleischhauer M. *et al.*, *Rev. Mod. Phys.*, **77** (2005) 633.
[3] Xu Q. F. *et al.*, *Phys. Rev. Lett.*, **96** (2006) 123901.
[4] Zhang S. *et al.*, *Phys. Rev. Lett.*, **101** (2008) 047401.
[5] Yang X. D. *et al.*, *Phys. Rev. Lett.*, **102** (2009) 173902.
[6] Yang Y. M. *et al.*, *Nat. Commun.*, **5** (2014) 5753.
[7] Gramotnev D. K. and Bozhevolnyi S. I., *Nat. Photon.*, **4** (2010) 83.
[8] Chai Z. *et al.*, *Adv. Opt. Mater.*, **2** (2014) 320.
[9] Zhang Z. R. *et al.*, *Appl. Phys. Lett.*, **104** (2014) 231114.
[10] Wang T. *et al.*, *Opt. Express*, **22** (2014) 21529.
[11] He Z. H. *et al.*, *Opt. Lett.*, **39** (2014) 5543.
[12] Lai G. *et al.*, *Opt. Express*, **23** (2015) 6554.
[13] Han Z. H. and Bozhevolnyi B. S., *Opt. Express*, **19** (2011) 3251.
[14] Huang Y. *et al.*, *Appl. Phys. Lett.*, **99** (2011) 143117.
[15] Cao G. T. *et al.*, *Opt. Express*, **23** (2013) 6554.
[16] Lu H. *et al.*, *Sci. Rep.*, **5** (2015) 8443.
[17] Cheng H. *et al.*, *Appl. Phys. Lett.*, **103** (2013) 203112.
[18] Shi X. *et al.*, *Opt. Express*, **21** (2013) 27438.
[19] Ding J. *et al.*, *Sci. Rep.*, **4** (2014) 06128.
[20] Wang L. *et al.*, *Opt. Express*, **19** (2014) 32450.
[21] Zeng C. *et al.*, *Appl. Phys. Lett.*, **105** (2014) 121103.
[22] Lu H. *et al.*, *Opt. Lett.*, **36** (2011) 3233.
[23] Lu H. *et al.*, *Phys. Rev. A*, **85** (2012) 053803.
[24] Wang L. *et al.*, *Opt. Lett.*, **40** (2015) 2325.
[25] Lu H., *Appl. Phys. B*, **18** (2014) 61.
[26] Li H. J. *et al.*, *EPL*, **104** (2013) 37001.
[27] Kekatpure R. D. *et al.*, *Phys. Rev. Lett.*, **104** (2010) 243902.